NUMERICAL AND EXPERIMENTAL SIMULATION OF A VERTICAL HIGH SPEED MOTORCOMPRESSOR ROTOR DROP ONTO CATCHER BEARINGS

David Ransom
Southwest Research Institute, San Antonio, TX 78238
david.ransom@swri.org
Andrea Masala
GE Oil&Gas, Centrifugal Compressors NPI Dept., Florence, 50127 Italy
andrea.masala@ge.com
Jeffrey Moore
Southwest Research Institute, San Antonio, TX 78238
jeff.moore@swri.org
Giuseppe Vannini
GE Oil&Gas, Conceptual & Advanced Mechanical Design Dept., Florence, 50127 Italy
giuseppe.vannini@ge.com
Massimo Camatti
GE Oil&Gas, Conceptual & Advanced Mechanical Design Dept., Florence, 50127 Italy
massimo.camatti@ge.com

ABSTRACT

A new research program was jointly set up between GE Oil&Gas and Southwest Research Institute (SwRI), to predict and test the dynamics of a vertical rotor drop on catcher bearings. A numerical tool able to account for flexible rotor and stator dynamics, catcher bearing stiffness and damping mechanism was developed. An experimental activity on a new vertical rotor test rig was carried out. A first analysis of numerical simulations and experimental analysis is presented in this paper.

INTRODUCTION

GE Oil & Gas has developed a hermetically sealed, high speed, high performance motor-compressor prototype for subsea applications.

The Active Magnetic Bearings (AMBs) technology together with a vertical rotor configuration and three radial bearings were identified as the best solution to meet both rotordynamic and subsea environment specific requirements.

The motor compressor AMBs are provided with catcher bearings to sustain the rotor in case of AMBs failure or temporary overloads.

Catcher bearings are a critical component because they must endure multiple impact-frictional contact forces with large acceleration, high rotational speed, radial overloads and must operate in harsh temperature conditions. In addition, during the drop phase, the rotor may experience a lateral self-excited vibration regime (backward/forward whirl), which can produce high dynamic loads on the bearings. In the case of a vertical axis machine, backward/forward whirl regime is even more likely to occur, because gravity load will not contribute to stabilize rotor position and prevent rotor whirl.

When the project started catcher bearing design and overall machine behaviour during the drop phase were identified as critical issues to get robust machine operation even in the case of AMBs failure and to be able to restart the machine after multiple landings without retrieving the entire unit from sea bed.

Most of landing technical knowledge has been developed for horizontal turbomachinery, while only few comparisons between predictions and measurements were performed for vertical units.

A detailed numerical model of vertical rotor drop on two catcher bearings, was developed by Sun et al.[1] to simulate the dynamics of a flywheel energy storage system on catcher bearings. The radial and axial rotor dynamics were combined in a 16 Degrees of Freedom (DOF) model, including cross-coupled stiffness and gyroscopic effects, and a parametric study on axial preload, friction coefficients and unbalance loads was carried out to highlight effects in terms of impact forces, heat generation and whirl rate prediction.

Experimental results of a 2MW vertical flywheel rotor drop on catcher bearings were presented by Caprio et al. [2]. The 44 drops performed highlighted the insurgence of forward motion for all unbalance level and drop speed conditions tested. Internal rotor damping, due to friction laminations stacks, was proposed as a possible origin of the forward acting force, in addition to

unbalance excitation. Forward whirl rate of the rotor close to the housing mode, suggested a strong effect of the combined rotor/stator system mode in determining the whirl "locking" frequency.

Similar tendency to forward rotor whirling was reported by Mc Mullen and al.[3] after an extensive 200 drops testing campaign on a 109 kg vertical flywheel rotor to identify drop dynamics and possible damage mechanism of catcher bearings and rotor.

As reported by Swanson et al.[4], the rotor unbalance level was experienced to be a key parameter in promoting the rotor forward whirl. Testing performed by the authors on different auxiliary bearing configuration and support system, showed the positive effects of compliance mounted auxiliary bearings to prevent whirl occurrence.

The behaviour of corrugated ribbon like (S2M design) damping system for compliance mounted catcher bearings, and effects in terms of rotor drop dynamics, were investigated by Schmied and Pradetto [5]. The numerical simulations and experimental activity highlighted the benefits of radial and circumferential damping, introduced by the corrugated ribbon, in limiting the whirl frequency and motion. Electromagnetic cross coupling forces due to motor stator and rotor interaction were suggested as possible origin of the unexpected forward rotor whirl experienced during the testing activity.

From literature above, concern on rotor whirl rate and direction, vibration amplitudes, and catcher bearings damage mechanism were deemed worth to be further addressed in order to close this technology gap for the vertical rotor drop prediction and identify suitable design solutions to leverage catcher bearing life (even further than API 617 7th Ed [6] expectations). Additional special features for this job are the presence of three radial bearings and the flexible rotor (unit running above first bending mode). A complete numerical and experimental approach was put in place to get a predictive tool able to analyse prototype performances and drive suitable design solutions.

The numerical part of the job consisted of a MatLab based code development to predict rotor drop behaviour through a non-linear transient simulation which takes into account both rotor and housing flexibility and catcher bearing non linear dynamics.

The final validation of this tool is performed through comparison with experimental data coming from a dedicated test rig built in SwRI facility.

Some of the experimental results coming from the first phase of this research activity are discussed in this paper.

NUMERICAL ACTIVITY

There are several key characteristics that determine the nature of the simulation. First, the landing event itself is a time transient event, and includes non-linear bearing supports due to the combination of the dead-band clearance in the auxiliary bearings, and the non-linear stiffness of the combined angular contact bearing pair and damper ribbon. Second, the geometry includes a flexible rotor and a casing with structural modes in the operating speed range. This requires fully flexible dynamic models of both the rotor and casing to be included in the simulation.

Component Models

In an effort to improve solution time, the flexible models of the rotor and casing have been dynamically reduced from their full form. The models are then coupled together by interface force equations, instead of the traditional direct stiffness approach. A general discussion of the analysis technique employed is provided by Ransom [7]. The casing model is developed in ANSYS® [8], and the reduced version is included in the simulation. The rotor model is also developed in ANSYS® and is reduced using the method published by Glasgow and Nelson [9]. The net model size reduction for both models is provided in Table 1. In total, the simulation model is reduced from a size of over 500,000 DOF to just 53 DOF.
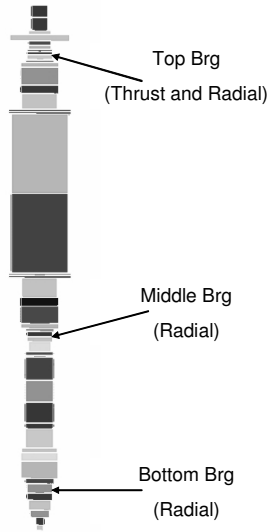
TABLE 1 : Model Reduction Results

Model	Full DOF	Reduced DOF	
	Physical	Physical	Modal
Casing	547,371	13	8
Rotor	378	22	10
Total	*547,749*	*53*	

As mentioned before, there are three auxiliary bearings in the test rig, and each are included in the simulation. The top bearing reacts both thrust and radial loads, while the middle and bottom bearings react only radial loads. Figure 1 shows the location of each of these bearings along the test rotor.

The bearing DOF are listed in Table 2. These are included in the simulation as independent DOF, and are determined from the mass properties of the actual bearing geometry.

TABLE 2: Bearing DOF

Bearing	Component	DOF
Top Bearing	Inner Race	X,Y,Z, θx
	Outer Race	Y,Z
Middle Bearing	Inner Race	Y,Z, θx
	Outer Race	Y,Z
Bottom Bearing	Inner Race	Y,Z, θx
	Outer Race	Y,Z

FIGURE 1: Bearing Locations Along Rotor

Top Brg
(Thrust and Radial)

Middle Brg
(Radial)

Bottom Brg
(Radial)

FIGURE 2: Auxiliary Bearing Assembly (S2M patent)

Structure

Damper Ribbon

Angular Contact
Bearing

Shaft

The top bearing includes the axial DOF (X), both lateral DOF (Y,Z) and the inner race spin DOF (θx) to track the rotational speed of the inner race. The outer race has only the two lateral DOF. The middle and bottom bearings are similar to the top, with the exception of the axial DOF, since there is no thrust reaction at these two bearings. Therefore, the total added DOF to represent the bearings is 16, raising the simulation DOF to 69.

All of the components of the analysis (rotor, casing, and bearings) are assembled into system level matrices, and cast into first order form. However, the component matrices remain uncoupled, with the connections between independent DOF accomplished via interface forces as outline by Ransom [7]. The assembled system is solved using readily available first order ordinary differential equation solvers. In this case, the second/third order adaptive Runge-Kutta solver is used (MatLab® ode23 [10]).

Interface Forces

Central to the success of the simulation is the calculation of the interface forces between the various simulation components. Figure 2 is a graphical representation of the auxiliary bearing assembly. The pair of preloaded angular contact bearings come in direct contact with the rotating shaft. This bearing pair is mounted within a preloaded ribbon damper, which is exaggerated in size for illustration purposes. Finally, the ribbon damper is mounted in a bearing housing that is bolted to the machine case.

There are three interface force locations considered in this simulation. First, at position one, there is direct contact between the rotor and the inner race. This contact results in both radial and tangential forces on both components. The radial interface force is calculated using Hertzian theory [11] as follows:

$$F_{R\_Hz} = \sqrt{\frac{K_D\, y^3}{\lambda_{hz}^3 C_E^{\,2}}} \tag{1}$$

Where K_D and λ_{hz} are functions of geometry, C_E is a function of material properties, y is the relative motion between the two bodies and F_{Hz} is the interface force between the two bodies. The tangential component is dependent on the relative rotation of the inner race and the shaft. If there is a difference in shaft spin speed, there is a net tangential force transmission. However, if the two speeds are equal (within a specified tolerance), the rolling contact condition is applied.

$$F_{T\_Hz} = \begin{cases} \omega_{IR} < \omega_{Rotor}\,, \mu_d F_{R\_Hz} \\ \omega_{IR} > \omega_{Rotor}\,, -\mu_d F_{R\_Hz} \\ \quad \omega_{IR} = \omega_{Rotor}\,, 0 \end{cases} \tag{2}$$

The interface forces at position two are determined from the angular contact bearing load/deflection curve (Figure 3). This curve includes the compliance of the angular contact bearing as well as additional compliance due to the kinematics of the bearing preload technique.
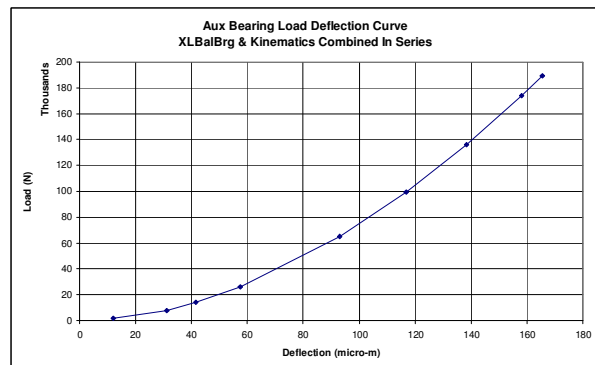
FIGURE 3: Auxiliary Bearing Load Deflection Curve

The third interface (position three) involves a somewhat bi-linear stiffness, with radial and tangential components. For the range of damper ribbon radial motion, the radial and tangential forces are calculated from a complex stiffness of the form:

$$F_{Dmpr} = yk_0 \left(1 + i\xi\right) \qquad (3)$$

Where k_0 is a function of ribbon geometry, and ξ represents the anticipated coefficient of friction. The real portion of this force is in the radial direction, while the imaginary component is in the tangential direction, opposing whirl. Clearly, the tangential component only has meaning when the outer race is whirling. Therefore, a condition is applied such that the tangential term must oppose the tangential velocity vector at any point in time.

Once the damper ribbon is fully compressed, the radial reaction force is the sum of the fully compressed damper spring force (real component) and the Hertzian contact force from the ribbon contact between the outer race and the bearing housing. This radial component is calculated using the same method as presented in Equation 1. The tangential force is still determined by the imaginary component of Equation 3.

Axial / Lateral Coupling

Another important interaction that must be captured is the axial/radial coupling which occurs at the thrust bearing location. When the rotor is in contact axially with the top bearing, there is an additional lateral friction force that tends to resist radial motion. The magnitude of the force depends on the interface force between the rotor and the bearing, and the coefficient of friction at this same interface.

There are three sources of compliance in the axial direction. First, there is a Hertzian contact stiffness between the rotor and the thrust bearing inner race. This is modelled similar to Sun et.al [1]:

$$K_{X\_hz} = \frac{E\sqrt{\pi\left(r_{ir}^2 - r_{or}^2\right)}}{0.96\left(1 - v^2\right)} \qquad (4)$$

Where E is material modulus, r_{ir} and r_{or} are the inner race inside and outside radii, respectively, and v is the material Poisson's ratio.

Second, the auxiliary bearing is supported axially by the preload spring with a known spring rate. Finally, the structure supporting the auxiliary bearing is also compliant. At each step of the integration, the resulting friction force at this interface is calculated, and applied opposite to the direction of motion of the rotor. In this way, the coupling between the axial and lateral directions is achieved.

Inner Race Spin Speed

As described above, the spin speed of each auxiliary bearing inner race is important to the tangential force calculations. Therefore it is important to include the effects of bearing drag torque and rotor/race interface torque. The drag (bearing friction) torque is modelled based on Harris [12]:

$$T_d = f_1 \left(0.9F_a \cot(\alpha) - 0.1F_r\right)d_m \qquad (5)$$

Where f_1 is a bearing design factor, F_a is the axial load, F_r is the radial load, α is the contact angle, and d_m is the bearing pitch diameter.
The friction torque is determined from the radial interface force between the rotor and the inner race, and the coefficient of friction.

EXPERIMENTAL ACTIVITY

Test Rig Description

The test rig consists of a three bearing rotor, suspended within a vertical casing (Figures 4 & 5). The primary bearings are AMBs from S2M, and provide control of seven axes (six radial and one axial) at three bearing locations. The secondary (Aux) bearings are pre-loaded pairs of angular contact bearings, also provided by S2M, and are supported in the radial direction by a damper ribbon from S2M. The test rig was built at one-third scale of the motor/compressor to minimize cost, but exhibits behaviour according to rotordynamic similitude. In order to have rotordynamic similitude, the test rig rotor will rotate at up to three times the full scale rotor, or about 30,000 rpm.
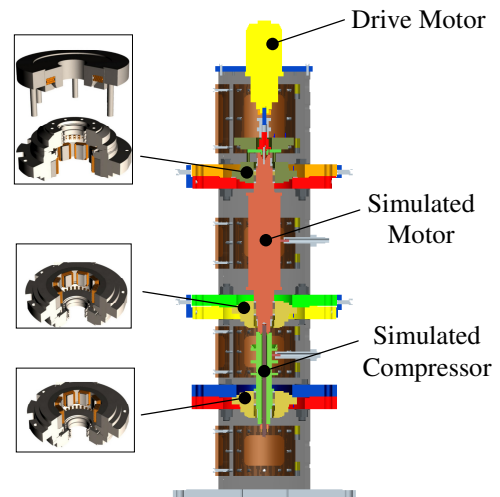

FIGURE 4: Vertical landing test rig

The test rig rotor is generally a 1/3 scale of the full scale unit, using dummy masses to simulate the permanent magnet motor core and the compressor impellers. The

test rotor is driven by an induction electric motor using a variable frequency drive (VFD), coupled via a flexible coupling to the top end of the motor-compressor assembly. This drive motor is used to accelerate the rotor to full speed and also used to slow down the rotor in a controlled fashion, matching as close as possible the anticipated rate of deceleration of the full scale unit.

In addition to AMBs sensors, two additional probes pairs are placed at rotor midspan planes to detect the rotor orbits in these planes. Four velocity transducers located on the casing at the upper and middle bearing plane locations are used to detect the housing dynamics. Transient data is captured using a 24 bit data acquisition system that acquires all 16 channels simultaneously DC coupled in a continuous waveform at 12,000 samples/sec.

FIGURE 5: Vertical rotor test rig at SwRI facilities

Test Parameters

The test matrix was designed to vary the following parameters: unbalance magnitude, unbalance distribution (to excite different modes), rotation speed, duration of the de-levitation, and which magnetic bearing axes were de-levitated. Two unbalance levels were tested, equating to about 4 and 12 times the API unbalance amount [6].

Test Results

Sample experimental results are presented in Figures 6, 7. These are waterfall plots of one of the axes at the top bearing location. All bearing axes exhibit similar behaviour.

Figure 6 shows the results from a drop starting at 20,000 rpm (12xAPI unbalance), and descending through the rotor bending mode at 300Hz. Re-levitation finally occurs 16 seconds later, at a shaft speed of about 15,000 rpm. The synchronous response is obvious, ramping from 333 Hz down to 250 Hz. Above the rotor bending

frequency, the whirl increases in frequency, ranging from 75 to 85 Hz. At the bending critical, the whirl frequency jumps to 100 Hz, and decays slightly to 90 Hz prior to re-levitation. The initial whirl amplitude is 600 μm pk-pk, increasing to 668 μm pk-pk at the critical speed. Just prior to re-levitation, the amplitude is reduced down to 646 μm pk-pk. It is important to note that even with this high level of unbalance, passage through the rotor bending critical is accomplished without difficulty on the auxiliary bearings. Although there is casing mode at 34 Hz, there is no sign of response at this frequency, demonstrating that the whirl frequency is not impacted by the presence of a casing mode within the operating speed range.
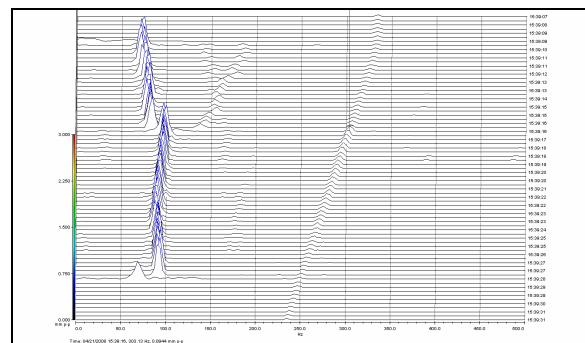
FIGURE 6: Drop from 20,000 rpm - Through 1st Bending Critical (Experiment)

The level of unbalance is then reduced to 4xAPI, and Figure 7 shows the results of a drop from 27,500 rpm. As a result of the much improved rotor balance, the synchronous response is not visible at this scale, and the amplitude and frequency of whirl are much reduced. The amplitude is limited to about 386 μm pk-pk, and the whirl frequency is around 63 Hz for the entire duration of the de-levitation.
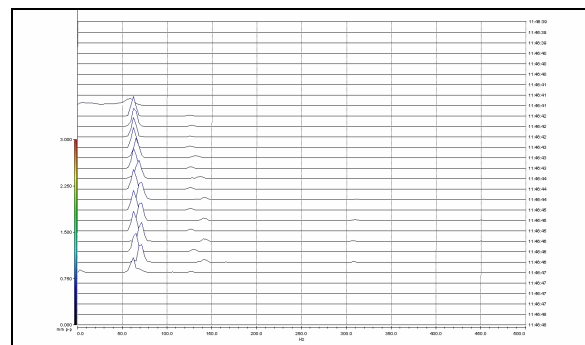

FIGURE 7: Drop from 27,500 rpm - Improved Rotor Balance (Experiment)

### COMPARISON OF EXPERIMENT AND SIMULATION RESULTS

This final section contains comparative results from both the experimental program and the numerical

simulation. The first point of comparison is the initial drop sequence, in which the rotor is free to travel through space until reaching the mechanical elements of the system. A vertical rotor lacks the radial gravity force which tends to suppress whirl. Figure 8 shows the initial drop trajectory for a drop speed of 21,500 rpm. The experimental results show that the rotor initially heads in the counter-clockwise (CCW) direction, consistent with the direction of spin. Additionally, it is clear from the orbit plot that the rotor proceeds directly into a forward whirl pattern, even after the very initial contact with the auxiliary bearings. The time duration represented by the orbit is 0.320 seconds, and the rotor establishes a whirl pattern in this period of time. In contrast, the simulation shows very little progression into whirl during the same period of time, and in fact shows the formation of backward whirl as the rotor makes contact with the auxiliary bearings.

(a)   (b)
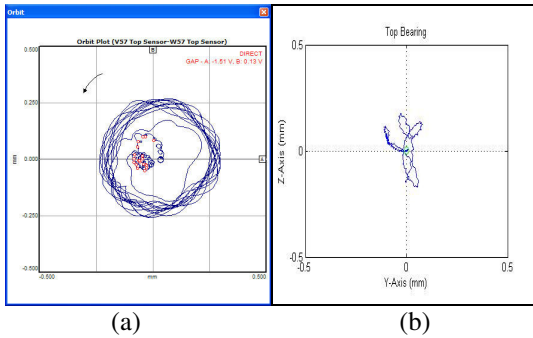
FIGURE 8: Initial Drop Trajectory from a) Experiment and b) Simulation (Spin Direction is CCW)

Figure 9 shows the steady state whirl after a few seconds of de-levitation. Notice that the experimental results show a smooth, steady whirl at an amplitude a little more than 500 μm pk-pk, consistent with the mechanical limits of the damper ribbon and the ball bearing clearance. The simulation shows similar amplitude of whirl, although not as smooth.


(a)   (b)
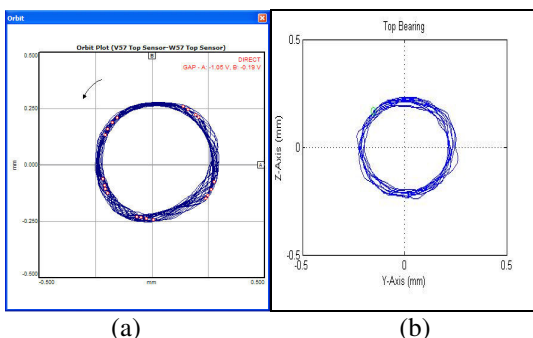
**FIGURE 9:** Steady Whirl from a) Experiment and b) Simulation

Figure 10 shows the displacement waveform associated with the steady whirl orbit for the experiment. The blue (dark) line represents the V axis, and the orange (light)

line represents the W axis. The direction of spin is from V to W, and it can be seen from this waveform data that the rotor is whirling in the forward direction (V leads W).

Figure 11 shows the displacement waveform from the simulation, and in this case the direction of spin is from Y to Z. The Z (solid line) is leading the Y (dashed line), indicating backward whirl.
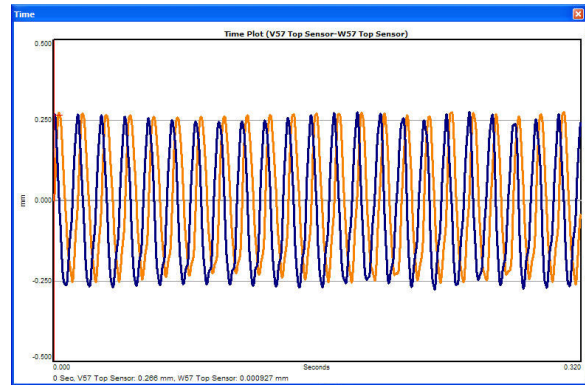

FIGURE 10: Forward Whirl at 70 Hz (Experiment)
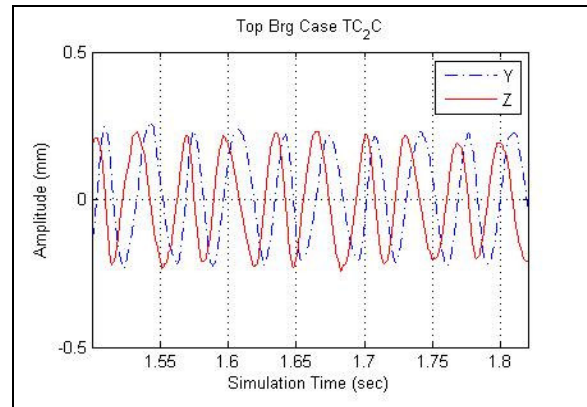
**FIGURE 11:** Backward Whirl at 28 Hz (Simulation)

Waterfall plots for both experiment and simulation are provided in Figures 12 and 13. The experimental results show the synchronous unbalance response starting at 358 Hz (21,500 rpm) and ending at 335 Hz at the end of the de-levitation period. The forward whirl observed in the time domain has an initial frequency of 70 Hz, progressing to 90 Hz by the end of the test.
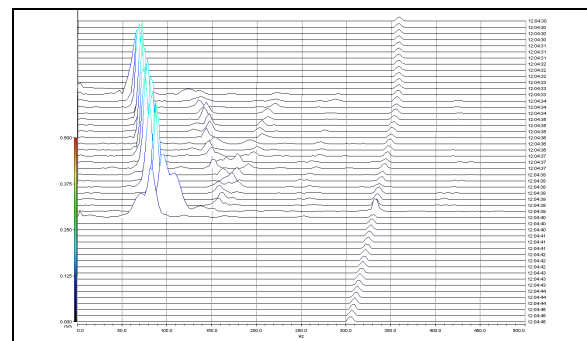
**FIGURE 12:** Drop from 21,500 rpm (Experiment)

The results from the comparable simulation show a much lower whirl frequency, initially at about 25 Hz. As time progresses, the backward whirl decays in both amplitude and frequency, eventually transitioning to forward whirl at about 25 Hz.

The results of this comparison indicate that there are forward whirl contributing forces missing from the simulation. As described above, the forces that contribute to whirl include the unbalance force vector (encouraging forward whirl) and the tangential interface force between the rotor and the auxiliary bearing (encouraging backward whirl). The experimental results show clearly that even at the time of impact, the rotor shows no tendency for backward whirl. However, at the first sign of impact in the simulation, the rotor is reflected into a backward whirl direction.
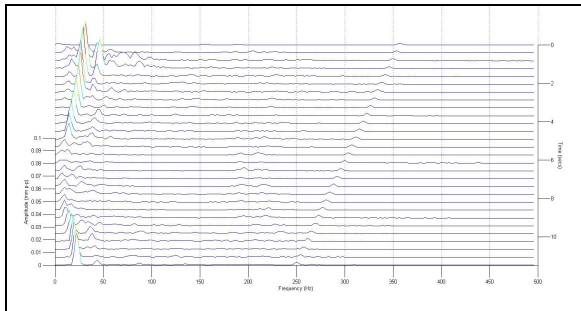
FIGURE 13: Drop from 21,500 rpm (Simulation)

In an effort to quantify the amount of forward whirl contribution necessary to match experimental results, additional cross-coupled stiffness is added to the simulation. Figure 14 (a & b) shows the orbit plots for the initial drop sequence for the both experiment and simulation. The simulation is performed with 3 N/μm of cross-coupled stiffness. The simulation drop transient now resembles the experimental results in that the rotor immediately enters forward whirl, and smoothly transitions to operation on the auxiliary bearings. There is no sign of the rotor "bouncing" off of the inner race at the time of first contact.


(a)   (b)
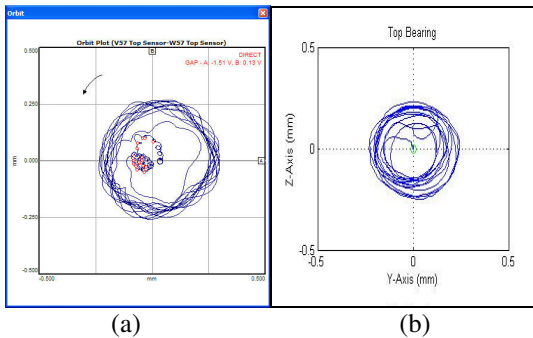
**FIGURE 14:** Initial Drop Trajectory - Effect of Added Cross-Coupling a) Experiment and b) Simulation

The steady whirl condition for both experiment and simulation is provided in Figure 15. With the additionally applied cross-coupled stiffness, the rotor exhibits a smooth whirl, much more like the experimental results.

Figure 16 shows the waveform of the simulated steady whirl condition, and it is clearly in forward whirl (Y leads Z).
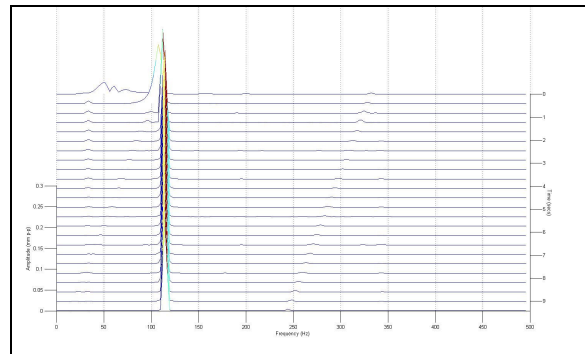
The waterfall plot (Figure 17) shows the whirl frequency stabilizing at about 110 Hz, which is slightly higher than the frequency of whirl in the experimental results.
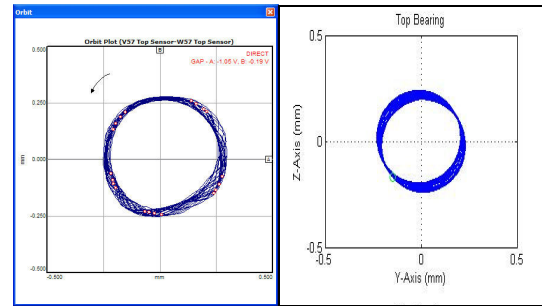
**FIGURE 15:** Steady Whirl - Effect of Added Cross-Coupling a) Experiment and b) Simulation
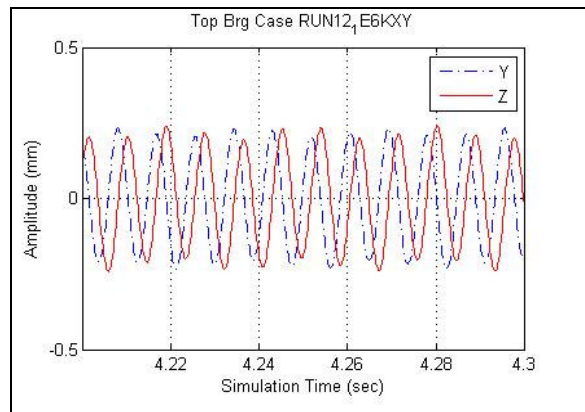
FIGURE 16: Forward Whirl at 110 Hz (Simulation, Kxy = 3.0 N/μm)

FIGURE 17: Drop from 20,000 rpm (Simulation, Kxy = 3.0 N/μm)

Performing the simulation again with one order of magnitude less cross-coupled stiffness (0.3 N/µm) results in a significantly lower whirl frequency (about 25 Hz), but it is still a forward whirl (Figure 18).
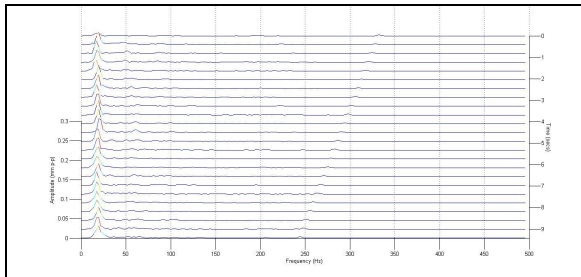
FIGURE 18: Drop from 20,000 rpm (Simulation, Kxy = 0.3 N/µm)

These results suggest that the final whirl frequency is not so much a function of support stiffness, but rather a function of the balance between the forces that contribute to whirl (both forward and backward) and the amount of energy dissipated by the auxiliary bearing system in the direction of whirl.

CONCLUSIONS

As a result of this combined analytical/experimental development program, some important conclusions can be made. The experimental results show excellent auxiliary bearing performance, even under very high unbalance conditions, and while passing through the rotor bending critical speed. This is encouraging, since long-duration operation without maintenance is a necessary feature of this sub-sea motor-compressor unit. Also, there is no sign of casing modes contributing to the dynamics of the whirl, so as long as the AMBs controller is tuned properly, there is no reason to anticipate added complications from the flexible casing. Comparative simulation runs indicate the presence of un-modelled cross-coupled terms, which are significant enough to drive the rotor into forward whirl, despite the backward whirl forces present during initial rotor/bearing contact. Simulation also shows the rotor response to be sensitive to the amount of cross-coupled stiffness. Therefore, it is important to consider this term in the design of a full-scale machine. Although it is usually not desirable to encourage forward whirl, in this case some positive cross-coupling is necessary to insure that the tangential rotor contact forces are not aligned with other negative cross-coupling terms, leading to a strong backward whirl.

Finally, further work is required to understand the sources of positive cross-coupled stiffness in this test rig. Possibilities include rotor friction from the assembled components, and gas dynamic forces at each of the close clearance auxiliary bearing locations.

References
1. Sun, G. et al., 2004, "Detailed ball bearing model for magnetic suspension auxiliary service," Journal of Sound and Vibration-269.
2. Caprio, M.T. et al.,2004, "Spin commissioning and drop tests of a 130kW-hr composite flywheel," Ninth International Symposium on Magnetic Bearings.
3. McMullen et al., 2006, "Flywheel Energy Storage System with AMB's and Hybrid Backup Bearings," Tenth International Symposium on Magnetic Bearings.
4. Swanson, E.E., Kirk, R.G., and Wang, J., 1995, "AMB Rotor Drop Initial Transient on Ball and Solid Bearings", UVA MAG.
5. Schmied, J. and Pradetto, J.C., 1992, "Behavior of a one ton rotor being dropped into auxiliary bearings," Third International Symposium on Magnetic Bearings.
6. API Std 617, 2002, "Axial and Centrifugal Compressors and Expander-compressors for Petroleum, Chemical and Gas Industry Services," Seventh Edition, American Petroleum Institute, July.
7. Ransom, D.L., 2008, "Leveraging the Strengths of Commercial Finite Element Modelling Codes and Custom Engineered Software to Solve Atypical Rotordynamic Problems", ASME TurboExpo.
8. ANSYS® Structural, Release 11.0, Help System, Advanced Analysis Techniques Guide, ANSYS Inc.
9. Glasgow, D. A., and Nelson, H. D., 1980, "Stability Analysis of Rotor-Bearings Systems Using Component Mode Synthesis," ASME Journal of Mechanical Design, Vol. 102, No. 2, Apr. , pp. 352-359.
10. MatLab® 7 Mathematics, The Math Works Inc., Natick, MA, USA, Ch. 6.
11. Young, W.C. and Budynas, R.G., 2002, "Roark's Formulas for Stress and Strain – Seventh Edition," McGraw-Hill, New York, NY.
12. Harris, T.A., 1984, "Rolling Bearing Analysis, 2nd Ed.," John Wiley and Sons, pp. 426-432.